Computers & Geosciences 106 (2017) 77–88

Contents lists available at ScienceDirect

Computers & Geosciences

journal homepage: www.elsevier.com/locate/cageo

Research paper

Learning characteristic natural gamma shale marker signatures in iron ore deposits

D. Nathan[a,*], P. Duuring[b], E.J. Holden[a], D. Wedge[a], T. Horrocks[a]

[a] Centre for Exploration Targeting, The University of Western Australia, 35 Stirling Highway, Crawley, WA 6009, Australia
[b] Geological Survey of Western Australia, Department of Mines and Petroleum, Mineral House, 100 Plain Street, East Perth, WA 6006, Australia

A B S T R A C T

Uncertainty in the location of stratigraphic boundaries in stratiform deposits has a direct impact on the uncertainty of resource estimates. The interpretation of stratigraphic boundaries in banded iron formation (BIF)-hosted deposits in the Hamersley province of Western Australia is made by recognizing shale markers which have characteristic signatures from natural gamma wireline logs. This paper presents a novel application of a probabilistic sequential model, named a continuous profile model, which is capable of jointly modelling the uncertainty in the amplitude and alignment of characteristic signatures. We demonstrate the accuracy of this approach by comparing three models that incorporate varying intensities of distortion and alignment in their ability to correctly identify a shale band of the West Angelas member of the Wittenoom Formation which overlies the Marra Mamba Iron Formation in the Hamersley Basin. Our experiments show that the proposed approach recovers 98.72% of interpreted shale band intervals and importantly quantifies the uncertainty in scale and alignment that contribute to probabilistic interpretations of stratigraphic boundaries.

1. Introduction

In the assessment of mineral resources the separation of a deposit in to geological domains is crucial to its feasibility. Moreover, the tendency of specifying domains based only on grade and not in unison with other geological parameters such as stratigraphic relationships and geometry can have detrimental consequences in final reserve estimates (Srivastava, 2005). This can be more apparent in the estimation of tabular ore bodies, such as stratiform iron ore bodies, where blocks are commonly unfolded so that stratigraphic contacts are horizontal before geostatistical estimation (Sommerville et al., 2014; Abzalov, 2016). The Hamersley province in Western Australia presents (Fig. 1) a useful case where the stratigraphic interpretation of drill holes can be constrained by the natural gamma signature of the borehole and is thus routinely collected in the exploration of the region (Jones et al., 1973; Kneeshaw et al., 2003). The Brockman and Marra Mamba iron formations are interbedded with shale bands that are laterally consistent across the province and that have distinctive peaks in the natural gamma signatures that are preserved through the enrichment process. This has allowed standard references of natural gamma responses for the mineralised sections of the Hamersley group to be developed which have been used to correlate sections spread across some 300 km (Jones et al., 1973; Blockley, 1979; Blockley et al., 1993). Moreover, given the gamma logs use in correlating horizons between drill holes, they also play a crucial role in evaluating the structural setting of a deposit and hence their interpretation has a large impact on the specification of the geological domains used in resource estimation (Sommerville et al., 2014).

Natural gamma logs measure the radioactivity from naturally occurring uranium, thorium and potassium (Russell, 1941). While these elements are generally found in higher concentration in shales, accounting for non-shale sources of natural gamma and the effect of grain size is important when interpreting the logs (Rider, 1990). There are also systematic variability for a given natural gamma shale peak that can be caused by numerous geological factors, including surface hydration from weathering, deformation, lateral discontinuities, variations in depositional energy, and sediment supply (Rider, 1996). The natural gamma peaks of the Hamersley Group in the Pilbara, Western Australia, have been shown to have a pattern that is consistent with the stratigraphy of the region and are therefore considered a reliable indicator for marker shale bands in the region (Murphy and Silversides, 2017). For iron ore deposits hosted in the Hamersley Group the enrichment of unmineralised banded iron formation (BIF) to ore occurs through the oxidation and replacement of primary magnetite and chert bands respectively that interbed the marker shale bands (Clout and Simonson, 2005; Thorne et al., 2008). In Brockman-

* Corresponding author.
E-mail address: david.nathan@uwa.edu.au (D. Nathan).

http://dx.doi.org/10.1016/j.cageo.2017.06.001
Received 10 February 2017; Received in revised form 26 April 2017; Accepted 1 June 2017
Available online 04 June 2017
0098-3004/

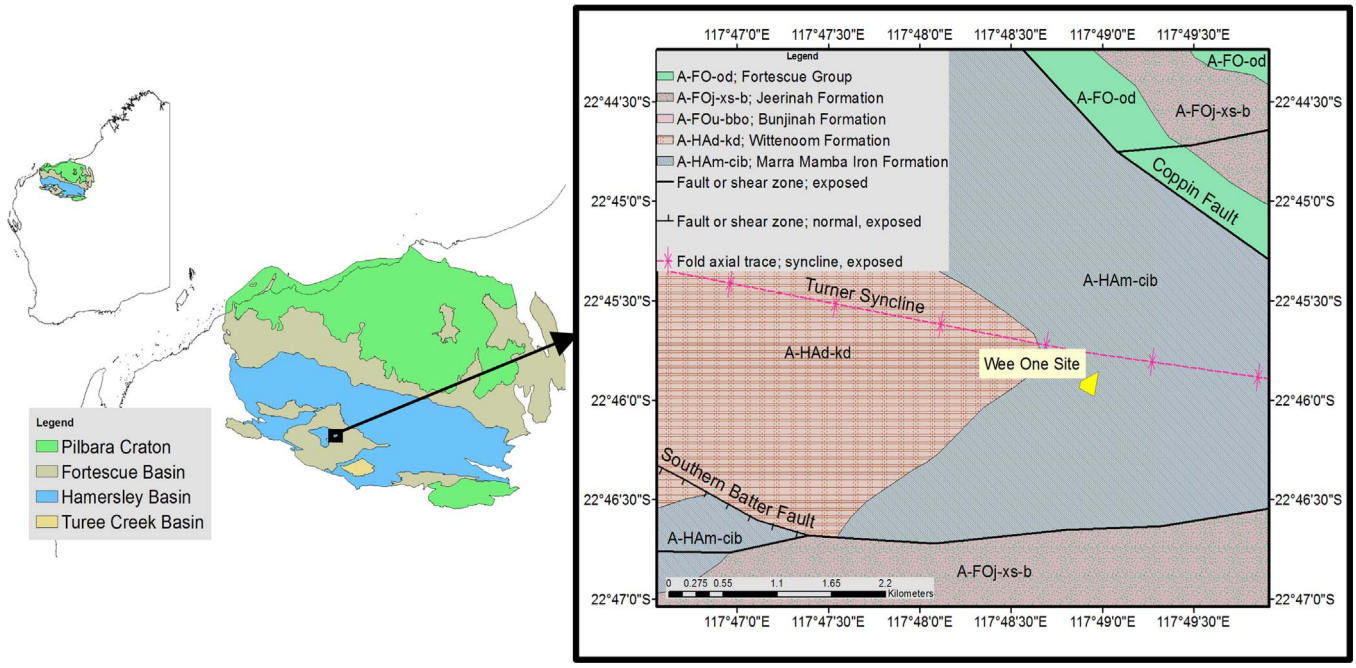

Fig. 1. Hamersley province geology (Geological Survey of Western Australia, 2016).

hosted ore bodies, this has the effect of thinning the stratigraphy due to the volume loss associated with hydrothermal alteration, ultimately causing variations in the distance between marker shales complicating their identification (Taylor et al., 2001). Similar complications also arise in Marra Mamba-hosted ore bodies where volume loss is associated with supergene alteration (Clout, 2006). Additionally, localised folding and faulting also distorts and misaligns gamma signatures (Jones et al., 1973) so that manual interpretation can be labour intensive and difficult to reproduce.

Previous work has focused on classifying gamma signatures corresponding to shale bands and building training libraries using Gaussian Processes (GP) (Silversides et al., 2011, 2015a; Silversides and Melkumyan, 2016a) combined with Dynamic Time Warping (DTW) (Silversides et al., 2015b; Silversides and Melkumyan, 2016b). Silversides et al. (2015a) used the standard deviation of the stochastic process underlying the signatures to drive an active learning approach to identify uncertain signatures. These uncertain signatures were then used to incrementally build a library of positive and negative examples used to classify an 8 m interval. While this approach is effective in modelling variations in signal amplitude, highly deformed and misaligned signals—which are common in wireline logging—in the training library can adversely affect its performance. To address this Silversides et al. (2015b) combined the output from the DTW and GP as a weighted sum for a prediction, which improved performance but could not quantify uncertainty, and thus could not be used for active learning. Uncertainty quantification was introduced by Silversides and Melkumyan (2016b) using DTW distances rather than Euclidean distances in the covariance function of the GP, which modelled the distortion and variability in scale.

In this paper, we demonstrate how the variability in scale and distortion can be jointly modelled in a single probabilistic graphical model framework (Wainwright and Jordan, 2008). This involves the novel application of a probabilistic sequence alignment model that can create a single characteristic representation of a shale marker signature from multiple gamma signatures. We apply a *continuous profile model* (CPM) (Listgarten et al., 2004) that is able to incorporate parts of a shale marker signature that are present in one sample but not another by modelling the probability of states defined by the *scale* and *sequence position* of a characteristic signature. An analogous approach is often used in bioinformatics where a probabilistic profile of a protein family is modelled using a *profile hidden Markov model* (profile HMM) (Durbin, 1998). The alignment of a protein can then be made by modelling the probability of a deletion, insertion or match state in a sequence of amino acids. This is similar to the alignment of natural gamma characteristic signatures in the Hamersley, where less competent shale bands are interbedded with more competent BIF. Thus, the probability of localised stretching and scaling in the characteristic signature as a result of folding or faulting will be based on the position within the signature.

A common application of Markov chains in geology is for the analysis of cyclic successions in stratigraphy (Doveton, 1971) and spatial Markov chains in geostatistics (Carle and Fogg, 1997) . Applications of hidden Markov models have mostly been limited to lithology (Jeong et al., 2014) or facies prediction (Eidsvik et al., 2004; Lindberg and Grana, 2015) where hidden states represent lithology types and observed values are petrophysical measurements. Other geological settings where automated lithology interpretation methods from petrophysics have been developed include coal deposits (Borsaru et al., 2006; Horrocks et al., 2015), carbonate sedimentary environments (Chang et al., 2000; Qi and Carr, 2006; Insua et al., 2015) , and shale-gas plays (Wang and Carr, 2012; Schlanser et al., 2016). The goal of natural gamma shale band signature characterization in iron ore deposits differs from the lithology and facies labelling problem in that the unobserved variable models how an observation is related to some canonical representation of the signal, and is thus more closely related to the problem of protein sequence alignment (Durbin, 1998). In a profile HMM, as applied in protein sequence alignment, the hidden state sequence represents operations that relate the observed sequence to a consensus sequence through operations such as insertion, deletion or matching. Analogously, in a CPM we relate an observed sequence to what we call the characteristic signature through the hidden state sequence. To our knowledge, the only existing work on probabilistic sequence alignment in the geoscience literature is Lin et al. (2014) who applied a profile HMM to align the sedimentation rates between ocean sediment core.

This paper presents a study that focuses on modelling highly variable gamma signature of the West Angelas shale member of the Wittenoom Formation which overlay the Marra Mamba Iron

Formation in the Hamersley Basin, Western Australia. To validate the effect of misalignment, we compare three models of the West Angelas AS1-AS2 shale member signatures: an unaligned average model, a smooth aligned CPM, and a distorted aligned CPM. The unaligned average model is calculated as the average of all the signatures once they have been linearly interpolated to same length. The distorted model is trained on gamma signatures from all holes while the smooth model excludes the gamma signatures known a priori to be highly distorted. The three models are then used to identify a section from a drillhole's complete gamma log by finding the minimum DTW measure (Sakoe and Chiba, 1978) with a specific aim to generate a horizon of the shale member. The uncertainty of the identified interval compared to the model is then assessed using the DTW distance, warping factor and log MAP Viterbi score (Forney, 1973) with the distorted model. A diagram of this workflow highlighting the elements that are probabilistically modelled and the elements that are deterministic is outlined in Fig. 2. The remainder of the paper is structured as follows: first, we summarise our dataset; second, we outline the methods and results for the modelling of the characteristic signature; third, we present the methods and results for identifying intervals using the models; and fourth, we provide a summary and future work.

1.1. Dataset

Our study used drill hole data from 11 exploration holes that cover parts of the Turner Syncline within the Hamersley province. The data has been made freely available by the Western Australian Department of Mines and Petroleum.[1] Their locations on a NearMap[2] aerial image are displayed in Fig. 3.

The data consists of 662 m of reverse-circulation drillholes that were chemically sampled at 2 m intervals. The geophysical wireline logs were measured at 10 cm intervals and included the natural gamma, the gamma-gamma bulk density, magnetic susceptibility and resistivity. A plot of the natural gamma logs in 3D is displayed in Fig. 4 with the interpreted signatures for the AS1 and AS2 markers of the West Angelas member in red.

2. Methods

2.1. Modelling shale marker signature

Since the *Continuous Profile model* (CPM) extends the concept of *Hidden Markov model* (HMM) which is widely used in time series data analysis, especially in the area of speech recognition (Rabiner, 1989). We first outline the theory of HMMs before introducing the CPM.

2.1.1. Hidden Markov chain model

A hidden state sequence model is one where each observation (e.g., a gamma emission) in a sequence $X=\{x_1, x_2, \ldots, x_N\}$ of length N has a corresponding state, i.e., there exists a state sequence $Z=\{z_1, z_2, \ldots, z_N\}$ that is not directly observed. Fig. 5a illustrates how a continuous-valued observed sequence of length $N = 10$, i.e. a natural gamma log, can be mapped to an unobserved state sequence. Each hidden state variable z is a discrete variable that has $K = 3$ possible values, {L,M,H}, which in this example represents low, medium and high. The motivation for using a hidden state is that the optimal parameters that fit some observed data Xwould be easier to compute if some intermediary variable Z were already known. In our example this is demonstrated by the fact that if we knew that an observation was low, medium or high, it would be easier to compute the optimal parameters, for example the mean μ and standard deviation σ of a Gaussian distribution. In a HMM, the probability distribution of a state z_n depends on the previous state z_{n-1} only and therefore is given by $p(z_n z_{n-1})$. The possible state transitions for the example are illustrated in Fig. 5b, where the edge labels represent the probability of changing from state i to state j, so that $A_{ij} \equiv p(z_n = j z_{n-1} = i)$. The transition matrix A in Fig. 5c demonstrates how an estimate for the transition probabilities can be calculated from the transition frequency divided by the total for the row.

The joint probability over all observations and states $p(x_{1:N}, z_{1:N})$ can be calculated as

$$p(x_{1:N}, z_{1:N}) = p(x_1, \ldots, x_N, z_1, \ldots, z_N) = p(z_1)\left[\prod_{n=2}^{N} p(z_n z_{n-1})\right]\prod_{n=1}^{N} p(x_n z_n). \tag{1}$$

The three probabilities that need to be inferred are: $p(z_1)$ the initial state probability distribution, $p(z_n z_{n-1})$ the state transition probability distribution and $p(x_n z_n)$ the emission probability distribution. The parameters that need to be learnt for the three probabilities are: the initial state priors π, the transition probabilities matrix A, and the emission density parameters θ. Thus, an HMM is fully specified by the set of parameters $\lambda = \{\pi, A, \theta\}$.

In standard formulations of HMM the values for λ are learnt using expectation-maximization (EM) (Dempster et al., 1977) which is also known as the Baum-Welch algorithm (Baum et al., 1970). The algorithm finds that λ which maximizes the log-likelihood $\log p(x_{1:N}\lambda)$ for the observed data. The EM algorithm starts with an initial selection for the model parameters λ^{old}. The E-step of the algorithm infers the posterior distribution for each z_n where $1 < n < N$ using the initial estimate ofλ^{old} by Bayes' rule:

$$p(z_n x_{1:N}, \lambda^{old}) = \frac{p(z_n, x_{1:N}\lambda^{old})}{p(x_{1:N}\lambda^{old})} = \frac{p(z_n, x_{1:N})}{p(x_{1:N})} \tag{2}$$

The conditional dependencies as illustrated in Fig. 6a allow the joint marginal distribution $p(z_n, x_{1:N})$ to be factored into component $\alpha(z_n)$ and $\beta(z_n)$ that can be recursively defined as

$$p(z_n, x_{1:N}) = \underbrace{p(z_n, x_{1:n})}_{\alpha(z_n)}\underbrace{p(x_{n+1:N} z_n, x_{1:n})}_{\beta(z_n)}. \tag{3}$$

This allows the exact inference of the posterior distribution to be efficiently calculated and is named the forward-backward algorithm (Rabiner, 1989). The M-step then maximizes the log-likelihood $\log p(x_{1:N}\lambda^{old})$ with respect to eachλ^{old} to update the parameter values to λ^{new} which are used in the next iteration. The algorithm terminates when the change in the log-likelihood is below a certain threshold.

The conditional dependencies between successive z_n imply that the most probable sequence of states $z_{1:N}$ for a given observation $x_{1:N}$ is different from the set of states that give each maximum posterior distribution $p(z_n x_{1:N})$. Instead the Viterbi algorithm (Forney, 1973), which is a recursive backward maximizer, can be used to calculate the maximum a posteriori (MAP) probability estimation of the state sequence:

$$\log \text{MAP Viterbi score} \equiv \max_{z_{1:N}} p(z_{1:N} x_{1:N}). \tag{4}$$

It can be derived from the observation in Eq. (1) that for a fixed$x_{1:N}$, the value of the last hidden variable z_N that maximizes the joint probability, i.e. $\max_{z_N} p(x_{1:N}, z_{1:N})$, only depends on the hidden variable z_{N-1} that precedes it. Thus, only K values (the size of the set of possible values for the hidden state) are necessary to evaluate what the most likely hidden state value is for any one position n. Each of these$K$values are thus recursively defined as $\omega(z_{n-1}) = \max_{z_n} p(x_n z_n) p(z_n z_{n-1})\omega(z_n)$ and is calculated for $2 \le n \le N$ with $\omega(z_N) = 1$. The most likely sequence of

[1] WAMEX A95838, *Wee One Annual Technical Report 2012* http://geodocs.dmp.wa.gov.au/search.jsp?Report_Ref=A95838 & cabinetId=2301.
[2] *Tom Price* 2012-08-15 http://www.nearmap.com.au/.

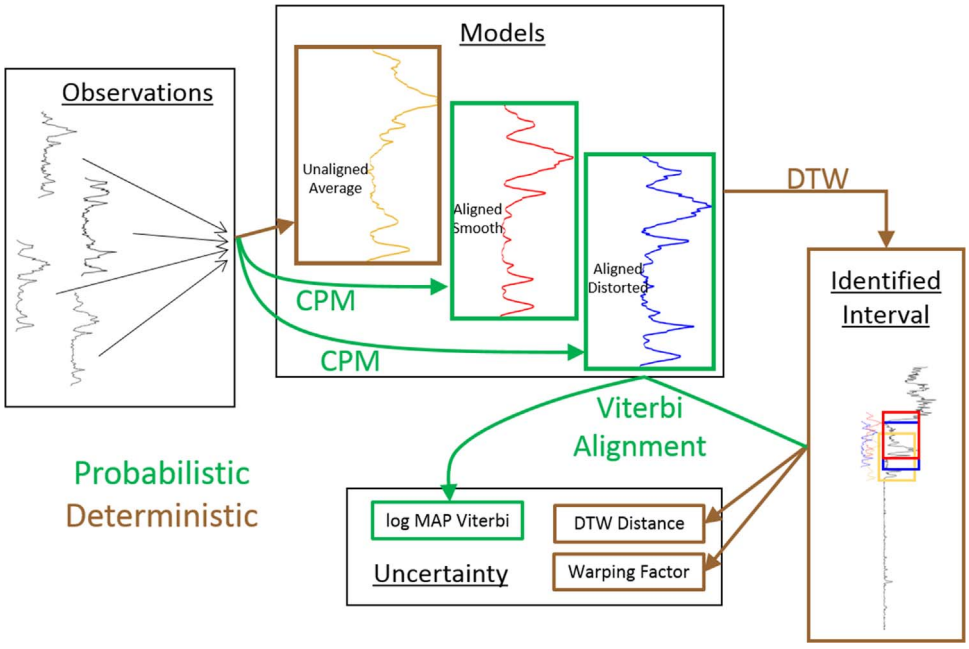

Fig. 2. An outline of the study workflow of generating the characteristic signature models, testing them by identifying the intervals that returns the minimal DTW distance, and analysing the uncertainty of the identified interval. Elements of the workflow that are probabilistically modelled are in green, and elements that are deterministic are in brown. (For interpretation of the references to color in this figure legend, the reader is referred to the web version of this article.)

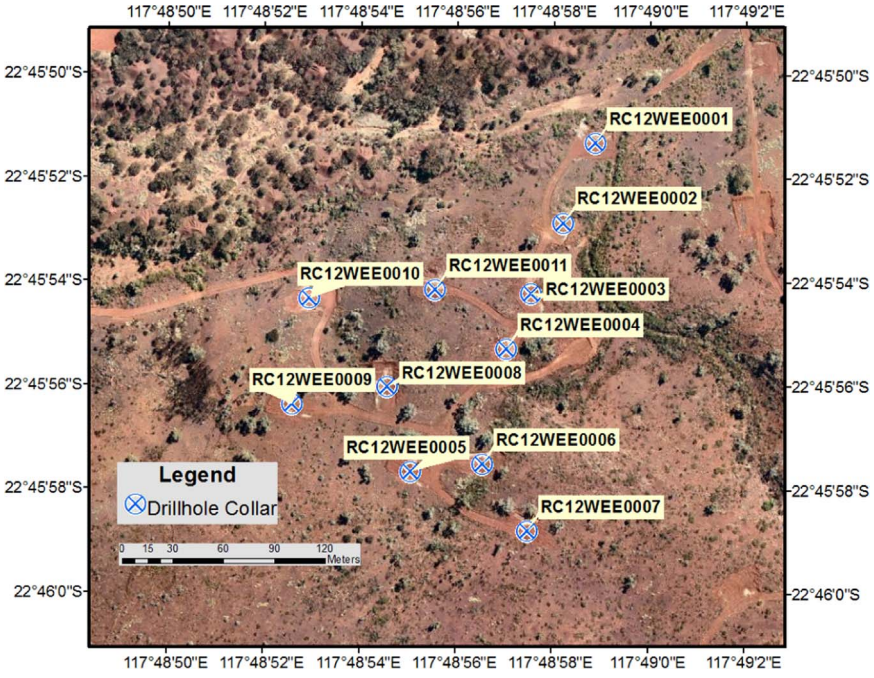

Fig. 3. Wee one site drill hole collar locations.

states then corresponds to evaluating $\tilde{\mathbf{z}}_n = \underset{z_n}{\text{argmax}} p(x_n z_n) p(z_n \tilde{\mathbf{z}}_{n-1}) \omega(z_n)$ where $\tilde{\mathbf{z}}_1 = \underset{z_1}{\text{argmax}} p(x_1 z_1) p(z_1) \omega(z_1)$.

2.1.2. Continuous profile model

The CPM extends the HMM so that there are two components for the hidden state z_n that correspond to a characteristic signature position state τ_n and scale state ϕ_n (Fig. 6b). This assumes that there exists a latent sequence $\tilde{t} = \{t_1, t_2, \ldots, t_M\}$ of length $M > N$ that represents the characteristic signature, of which, each observation sequence $X=\{x_1, x_2, \ldots, x_N\}$ is a noisy transformation. To accommodate the variations in alignment of the sample signatures, the length M of the characteristic signature $\tilde{t}$ must be larger than the number of observations N. The values that the variable τ_n can take are integers between 1 and M so that the set of possible values is $\tilde{\boldsymbol{\tau}} = \{1,2,\ldots,M\}$. The range of scaling ϕ_n is between $0.66 = 2^{-0.60}$ and $1.23 = 2^{0.60}$. We specify Q possible scale states so that are evenly spaced between −0.60 and 0.60 in logarithmic space, giving the set of possible values as $\tilde{\boldsymbol{\phi}} = \{(2^{-0.60})_1, (2^{-0.60+1/Q})_2, \ldots, (2^{0.60-1/Q})_{Q-1}, (2^{0.60})_Q\}$. This results in $K = QM$ possible states for z_n.

The state transition probability distribution $p(z_n z_{n-1})$ is separated into its scale state and characteristic signature position components so that $A_{z_{n-1},z_n} \equiv p(z_n z_{n-1}) = p(\phi_n \phi_{n-1}) p(\tau_n \tau_{n-1})$. The transitions between states are also restricted so that the characteristic signature position state τ_n can move forward by a maximum of J_τ positions and that the

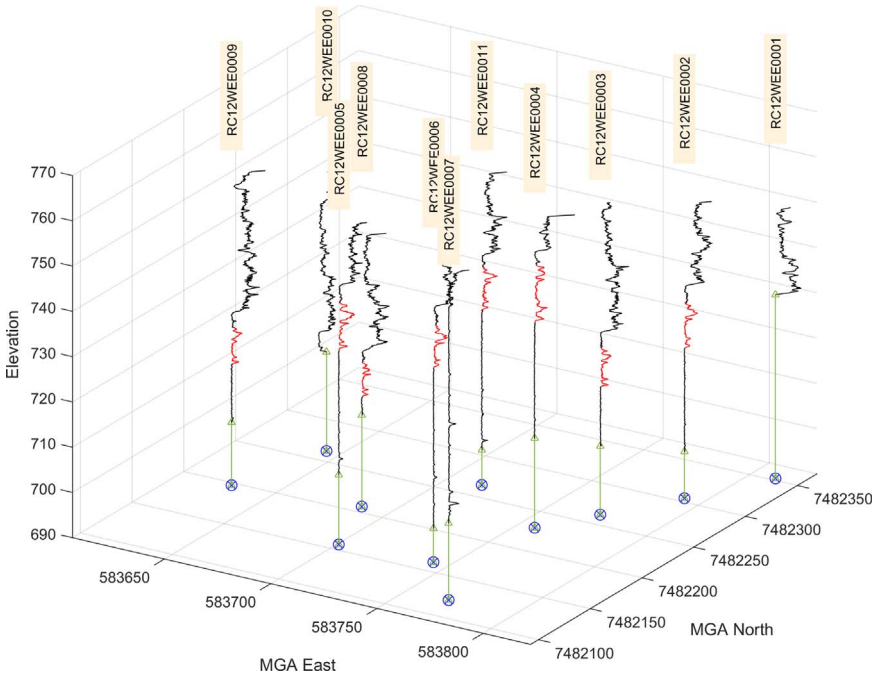

Fig. 4. Natural Gamma signatures facing NW with interpreted AS1-AS2 signatures in red. (For interpretation of the references to color in this figure legend, the reader is referred to the web version of this article.)

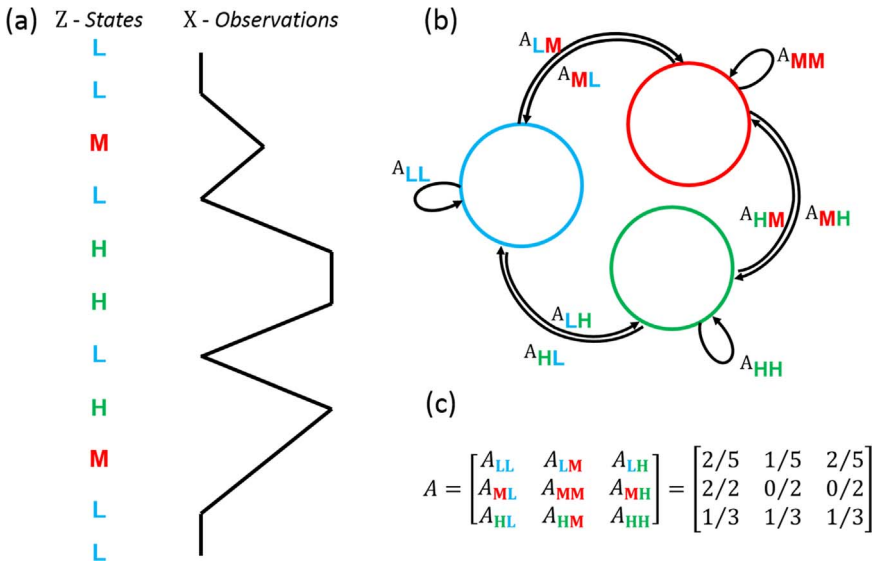

Fig. 5. (a) an example of a gamma log X of length $N = 10$ that has $K = 3$ states {L, M, H}, (b) the corresponding state transition diagram, (c) a transition probabilities matrix A that is calculated from the transitions in the state sequence Z.

scale state ϕ_n can only change in steps. The probability distributions of $p(\phi_n\phi_{n-1})$ and $p(\tau_n\tau_{n-1})$ are multinomials that maintain the transition restrictions such that

$$p(\tau_i = a|\tau_{i-1} = b) = \begin{cases} d_1, \ if\ a-b=1 \\ d_2, \ if\ a-b=2 \\ \vdots \\ d_{J_\tau}, \ if\ a-b=J_\tau \\ 0, \ otherwise \end{cases} \quad (5)$$

$$p(\phi_i = a|\phi_{i-1} = b) = \begin{cases} s_0, \ if\ a-b=0, \ no\ scale\ change \\ s_1, \ if\ a-b=1, \ scale\ increase\ by\ 1 \\ s_1, \ if\ a-b=-1, \ scale\ decrease\ by\ 1 \\ 0, \ otherwise \end{cases} \quad (6)$$

We empirically set the value of $J_\tau = 5$ and $Q = 9$. The value of M is set to twice the value of $N + \epsilon$ where we set $\epsilon = 0.1$.

The characteristic signature $\tilde{t}$ is incorporated into the model by adjusting the emission probability distribution so that the probability of the observation x_n is conditioned on $\tilde{t}$ and the observation noise level σ as well as the state z_n (see Fig. 6b). In the CPM model, since the observation X is assumed to be a scaled noisy transformation of the characteristic signature $\tilde{t}$, the emission probability distribution of each x_n is normally distributed with mean $\mu = t_{\tau_n}\phi_n$ and standard deviationσ which is the signal noise.

$$p(x_n z_n, \tilde{t}, \sigma) \equiv \mathcal{N}(x_n; t_{\tau_n}\phi_n, \sigma) \quad (7)$$

The emission probability distribution in Eq. (7) allows the EM algorithm to update the characteristic signature $\tilde{t}$ as any of the other

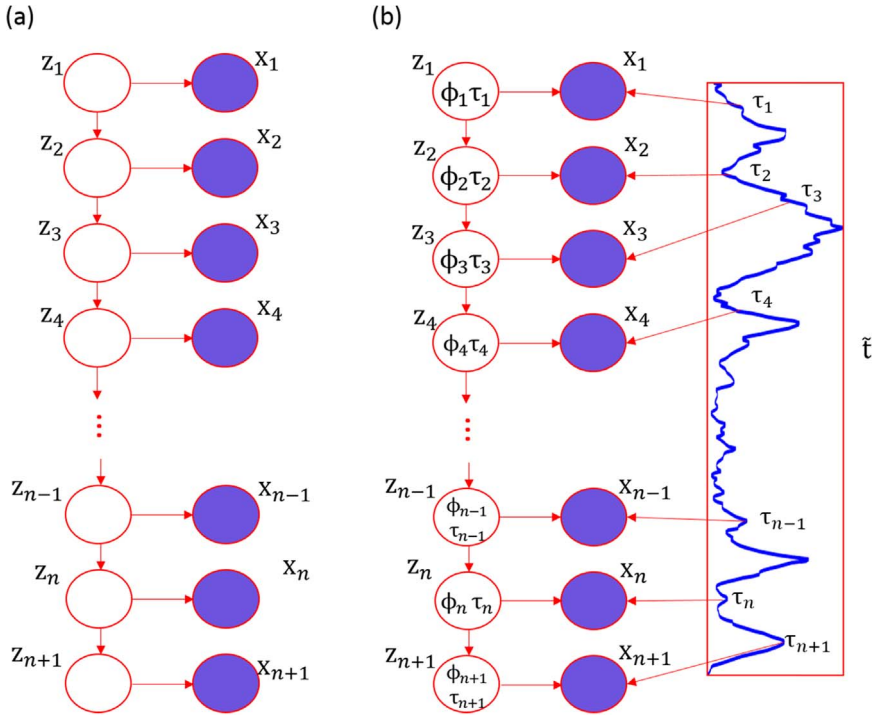

Fig. 6. (a) HMM graphical structure with hidden state variables z and observation variables x (b) CPM graphical structure where each hidden state variable z_n maps to a scale state ϕ_n and characteristic signature position stateτ_n, and where the observed value x_n is dependent on the characteristic signature $\tilde{t}$ as well as z_n.

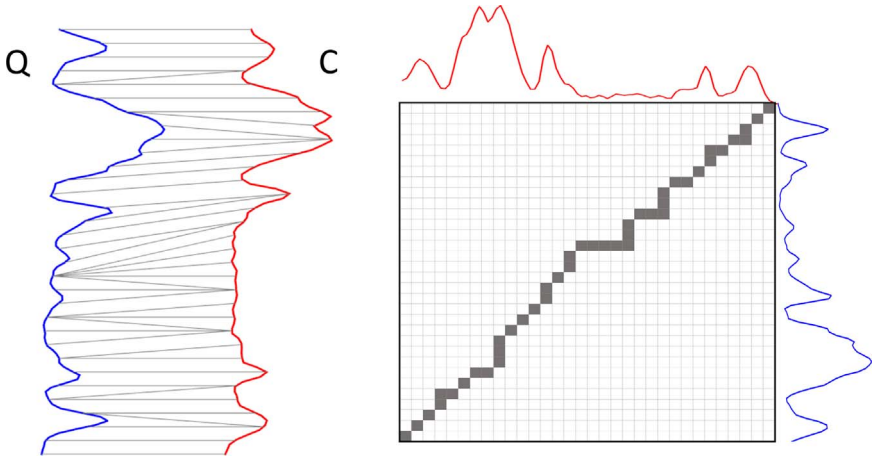

Fig. 7. (left) an example of DTW alignment between two gamma logs, (right) the optimal warping path through the distance matrix D.

parametersλ. The parameters for the CPM are thus$\lambda = \{\pi, A, \theta\}$, where the initial state priors π is a K dimensional vector, the transition probabilities A is a $K \times K$ matrix, and the emission density parameters θ are the characteristic signature $\tilde{t}$ and signal noise σ. The initial value of the signal noise σ is set as 15% of the range of values in the first observation in the training set. The initial characteristic signature $\tilde{t}$ is taken as the first observation in the training set with zero-mean σ^2-variance Gaussian noise added. This is upsampled to a length $2N$ by repeating each value twice, with the values at the ends corresponding to ε being set to the minimum value in the observation. The maximum a posteriori state sequence estimation that results from the Viterbi algorithm can then be used to align an observation to $\tilde{t}$ by applying the scale states $\phi=\{\phi_1, \phi_2, \ldots, \phi_n\}$ and characteristic signature position state $\tau=\{\tau_1, \tau_2, \ldots, \tau_n\}$. This implies that the scaling and aligning is not applied to the observation samples but are taken as scaled and aligned versions of the characteristic signature.

2.2. Testing the shale marker model

2.2.1. Dynamic time warping

Dynamic Time Warping (DTW) (Sakoe and Chiba, 1978; Keogh and Ratanamahatana, 2004) is a commonly used pattern matching algorithm that measures similarity between series that may have non-linear differences in alignment. We use DTW here to measure the similarities between the observed gamma logs and the model to demonstrate how the model could be used in prediction.

Given a query gamma log $Q = q_1, q_2, \ldots, q_N$ and a candidate gamma log $C = c_1, c_2, \ldots, c_N$ of length N, a $N \times N$ matrix D of the squared pairwise distance between the gamma values of Q and the gamma values of C is calculated, where the element $D(i, j)$ corresponds to the distance between q_i and c_j. A warping path $W = w_1, w_2, \ldots, w_K$ of length K is defined as a set of the matrix elements that is constrained by three conditions:

- The boundary condition: $w_1 = D(1,1)$ and $w_K = D(n, m)$ so that the start and end of each series are mapped to each other.
- The continuity condition: given $w_k = D(a, b)$ and $w_{k-1} = D(a',b')$, then $a - a' \leq 1$ and $b - b' \leq 1$ so that the path can only move in step changes.
- The monotonicity condition: given $w_k = D(a, b)$ and $w_{k-1} = D(a',b')$, then $a - a' \geq 0$ and $b - b' \geq 0$ so that the path can only move forwards. This is a geologically plausible constraint as there is no faulting or overturning present in the project area.

The optimal warping path is defined as the warping path that minimizes the accumulated distance (see Fig. 7). To compare the accumulated distances across different warping paths the distance is normalized by the length of the path K (see Eq. (8)).

$$DTW(Q, C) = \min\left\{\frac{\sqrt{\sum_{k=1}^{K} w_k}}{K}\right\} \tag{8}$$

Another measure that can be used to assess the optimal path is the warping factor which we use to compare the identified interval results across drillholes (see Eq. (9)), where N is the query and candidate sequence length and K is the warping path length.

$$WarpingFactor(Q, C) = \frac{N-K}{N} \tag{9}$$

To test the effectiveness of the learnt characteristic signal $\tilde{t}$ we use it to query each drillhole's natural gamma log to identify the section of the log that it is most like. A sliding-window of varying width was used to find the nearest-neighbour section by selecting the section with the smallest accumulated DTW distance. The window size varied from 6.0 – 16.0 m at 0.1 m increments. This was applied to all 11 holes including those from which no interpreted section was possible.

3. Results

The interpreted AS1-AS2 section from eight drillholes were used to train a characteristic signature. To compare the effect of distorted signatures on the trained model, a separate characteristic signature was learnt without the RC12WEE0004 section which is the most distorted signature (see Fig. 8d). The characteristic signature trained on all eight observations including RC12WEE0004 is described as the distorted model (Fig. 8c) and the characteristic signature trained without RC12WEE0004 is described as the smooth model (Fig. 8b). An unaligned model was also tested to compare against the aligned models. The unaligned *average* model was calculated by expanding each interpreted AS1-AS2 interval by linear interpolation to the length of the longest observation, and taking the average (see Fig. 8a).

The most likely aligned and scaled versions of the samples with the distorted model are presented in the middle of Fig. 9. EM training was run until the log-likelihood changed by a factor of at most 0.001. Each of the samples used in training were linearly interpolated to the length of the longest training sample. The scaled and aligned samples are taken as the Viterbi alignment of the observed samples on the right. The forwards-backwards algorithms has a time-complexity of $O(N \bullet K^N)$ where N is the length of the sequence and K is the number of possible states. The training of the 8 samples was approximately 9 min on a standard laptop computer running an Intel i7-4710HQ CPU at 2.50 GHz. The DTW algorithm has a time-complexity of $O(N^2)$. The identification of the section across all 11 holes was approximately 3 min on a standard laptop computer running an Intel i7-4710HQ CPU at 2.50 GHz.

The results of the identified horizons using the learnt characteristic signature are presented here in Tables 1 and Table 2.

The results of all identified sections are presented in Table 1. The total length of the intervals together with the overlap of the identified and actual intervals as a proportion of both the actual and identified interval are presented in Table 2. For the calculations in Table 2, let $[y^a_{\text{bottom}}, y^a_{\text{top}}] = \{x \in \mathbb{R} y^a_{\text{bottom}} \leq x \leq y^a_{\text{top}}\}$ be the actual shale marker interval and $[y^i_{\text{bottom}}, y^i_{\text{top}}]$ be the identified shale marker interval. The overlap of the two intervals is defined as $[y^o_{\text{bottom}}, y^o_{\text{top}}] = [y^a_{\text{bottom}}, y^a_{\text{top}}] \cap [y^i_{\text{bottom}}, y^i_{\text{top}}]$. The actual proportion is calculated as

$$\text{actual}\% = \frac{y^o_{\text{top}} - y^o_{\text{bottom}}}{y^a_{\text{top}} - y^a_{\text{bottom}}} \times 100\# \tag{10}$$

With the identified proportion calculated as

$$\text{identified}\% = \frac{y^o_{\text{top}} - y^o_{\text{bottom}}}{y^i_{\text{top}} - y^i_{\text{bottom}}} \times 100 \tag{11}$$

The overlap as a proportion of the actual interval can be interpreted as the true positive rate, and as a proportion of the identified interval can be interpreted as the complement of the false positive rate. The mean true positive rate (higher is better) for the average model was

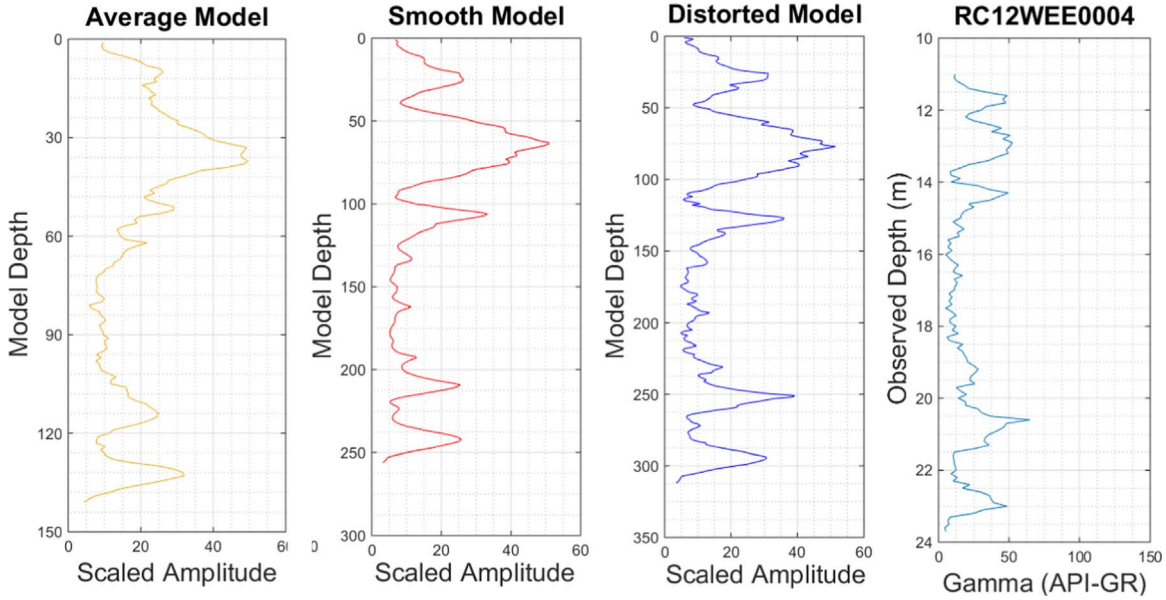

Fig. 8. (a) The average of the 8 signatures after they have been linearly interpolated to the longest signature (b) Smooth learnt signal trained without RC12WEE0004, (c) Distorted learnt signal trained with RC12WEE0004, (d) The distorted RC12WEE0004 AS1-AS2 signature.

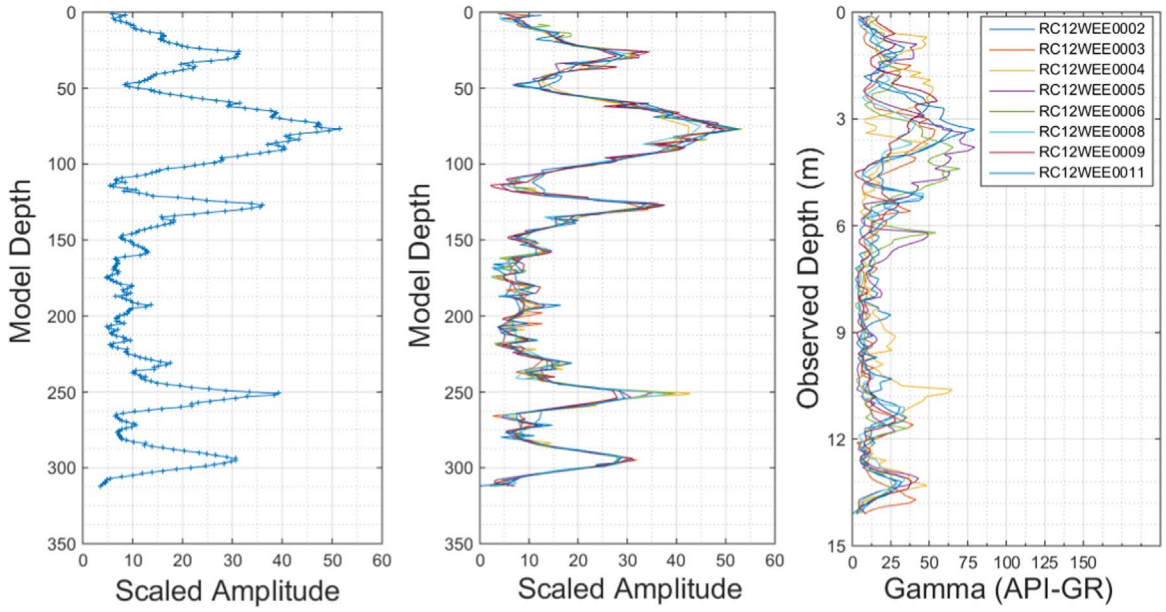

Fig. 9. (left) The learnt characteristic signal for the distorted model after training on 8 samples, (middle) Aligned and scaled versions of the samples with the distorted model, (right) The 8 unaligned unscaled samples used for training.

Table 1
Results of smallest accumulated DTW distance horizon identified with search window between 6.0–16.0 m. The bold rows correspond to the holes used in Fig. 10.

HoleID	AS2 top elevation (m)				AS1 bottom elevation (m)			
	Actual	Identified			Actual	Identified		
		Average	Smooth	Distorted		Average	Smooth	Distorted
RC12WEE0001	–	748.7	748.8	748.6	–	741.0	741.0	741.0
RC12WEE0002	733.2	733.6	733.5	733.5	723.0	723.1	722.9	722.7
RC12WEE0003	**727.1**	**726.7**	**726.5**	**727.0**	**718.4**	**718.1**	**719.6**	**718.2**
RC12WEE0004	**748.1**	**748.6**	**749.2**	**750.2**	**735.3**	**739.1**	**739.1**	**735.8**
RC12WEE0005	743.4	743.2	743.2	743.2	732.9	732.6	732.6	732.6
RC12WEE0006	742.5	742.1	742.2	742.1	733.0	732.8	732.7	732.7
RC12WEE0007	–	762.0	762.0	762.1	–	755.3	756.0	755.3
RC12WEE0008	**722.0**	**722.0**	**722.1**	**722.2**	**714.2**	**714.1**	**714.4**	**714.0**
RC12WEE0009	724.9	725.5	725.5	725.5	716.6	716.5	716.4	716.6
RC12WEE0010	–	735.7	740.3	740.3	–	729.0	734.3	734.3
RC12WEE0011	738.2	738.6	738.4	738.6	728.6	728.0	728.6	728.2

Table 2
The overlap of the identified and actual interval as a proportion of the actual and identified interval (higher is better). The bold rows correspond to the holes used in Fig. 10.

HoleID	AS1–AS2				Identified/actual					
	Total length (m)				Interval overlap					
	Actual	Identified			% of actual			% of identified		
		Average	Smooth	Distorted	Average	Smooth	Distorted	Average	Smooth	Distorted
RC12WEE0001	–	7.7	7.8	7.6	–	–	–	–	–	–
RC12WEE0002	10.1	10.5	10.6	10.8	99.08	100.00	100.00	95.61	95.59	93.82
RC12WEE0003	**8.7**	**8.6**	**6.9**	**8.8**	**95.57**	**78.99**	**99.01**	**97.07**	**100.00**	**98.28**
RC12WEE0004	**12.8**	**9.5**	**10.1**	**14.4**	**70.92**	**70.92**	**96.72**	**95.46**	**89.79**	**85.89**
RC12WEE0005	10.6	10.6	10.6	10.6	97.30	97.30	97.30	96.87	96.87	96.87
RC12WEE0006	9.5	9.4	9.6	9.5	96.70	97.75	96.70	97.77	96.77	96.74
RC12WEE0007	–	6.7	6.0	6.8	–	–	–	–	–	–
RC12WEE0008	**7.8**	**7.9**	**7.7**	**8.2**	**100.00**	**96.56**	**100.00**	**99.08**	**98.16**	**95.46**
RC12WEE0009	8.2	9.0	9.1	8.9	100.00	100.00	100.00	91.62	90.61	92.65
RC12WEE0010	–	6.7	6.0	6.0	–	–	–	–	–	–
RC12WEE0011	9.6	10.6	9.8	10.4	100.00	99.68	100.00	90.99	98.10	92.74

94.95%, for the smooth model 92.65%, and for the distorted model 98.72%. The mean false positive rate (lower is better) was 4.44% (0.43 m) for the average model, 4.26% (0.41 m) for the smooth model and 5.94% (0.66 m) for the distorted model.

The identified intervals for the three holes RC12WEE0003, RC12WEE0004, and RC12WEE0008 with their natural gamma wire-

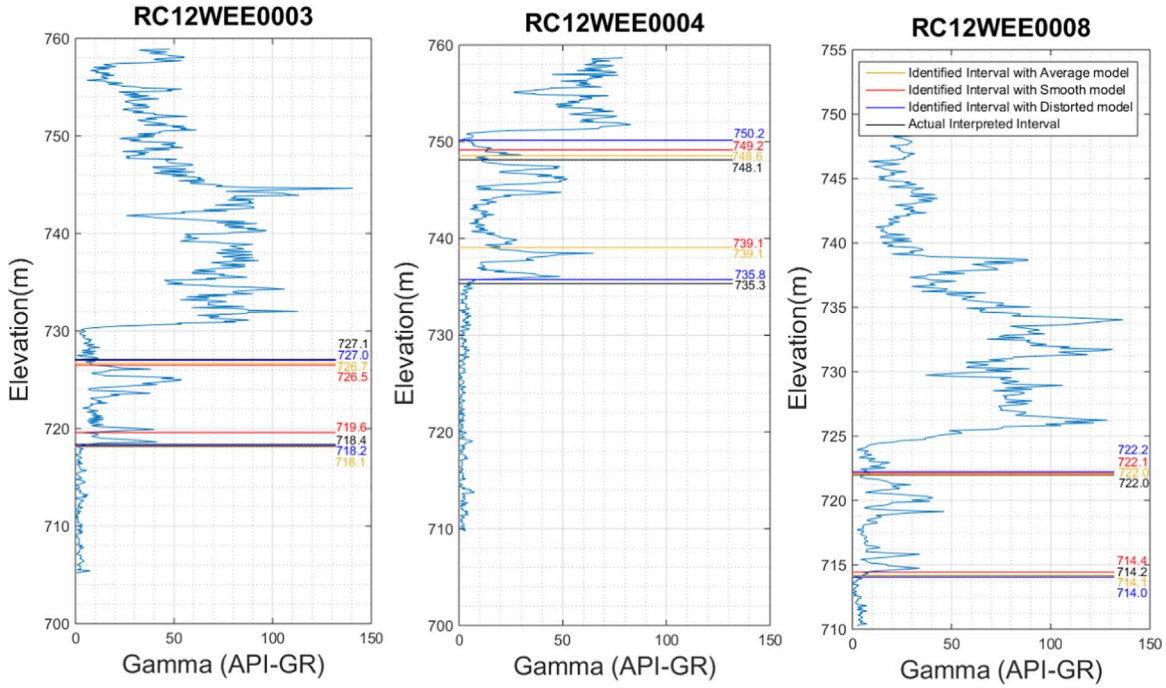

Fig. 10. Extracted AS1-AS2 interval for holes in the cross section using characteristic signature trained on all holes.

line logs are displayed in Fig. 10. While the inclusion of RC12WEE0004 in the distorted model does not improve or adversely affect the identified section in RC12WEE008, it has improved the identified sections in RC12WEE0003 and RC12WEE0004.

We also show a gridded 3D surface of the horizon in Fig. 11 calculated using the minimum curvature, together with a cross-section. The cross-section shows how the complex natural gamma signature for rocks intersected by the RC12WEE0004 drill hole is likely related to the presence of an antiformal fold hinge.

For the holes which did not contain the characteristic signature, the identified sections are presented in Fig. 12. Since the gamma logs in holes RC12WEE0001 and RC12WEE0010 are incomplete the identified sections do not appear to correspond to a likely AS1-AS2 section, while the identified section from RC12WEE0007 is likely to be the bottom of the West Angelas member.

The uncertainty analysis of the identified sections is presented in Table 3 using the DTW distance (see Eq. (8)), the warping factor (see Eq. (9)), and the log MAP Viterbi score (see Eq. (4)). We note that for gamma logs known not to contain the shale marker (RC12WEE0001, RC12WEE0007, and RC12WEE0010), the identified sections have the highest uncertainty across all gamma logs for four cases in Table 3: the DTW Distance for the Smooth and Distorted model, and the log MAP

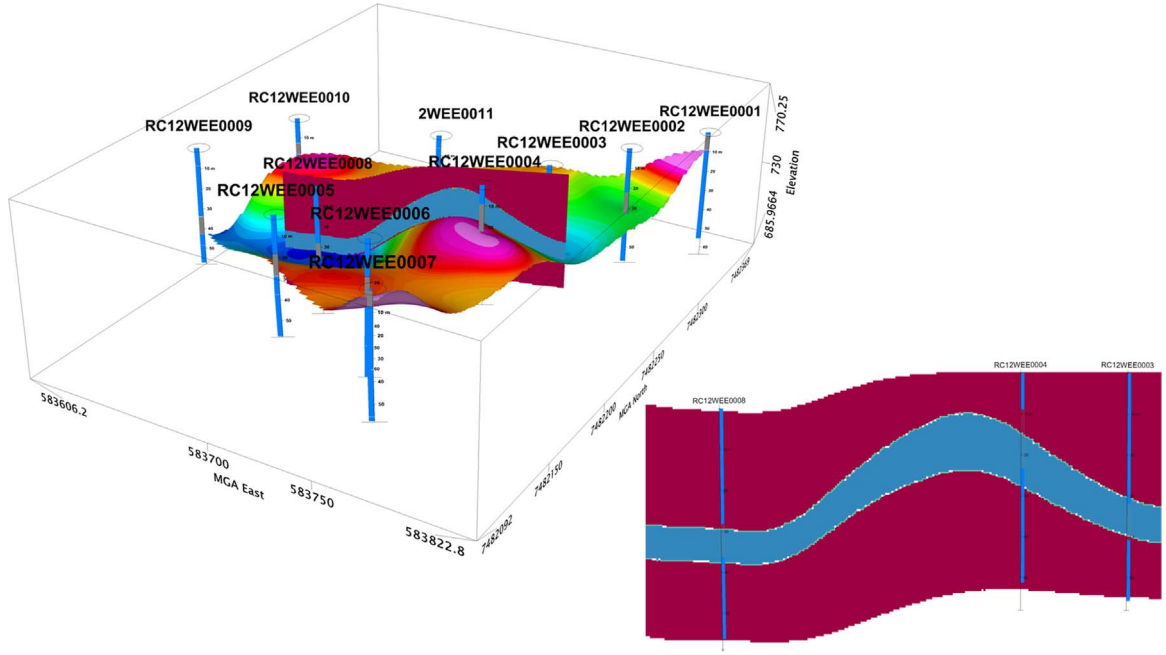

Fig. 11. (left) The bottom of the extracted AS1-AS2 marker surface and Cross-Section. NW facing. The colour of the surface corresponds to the elevation. (right) A cross-section of the surface showing where RC12WEE0004 is positioned compared to RC12WEE0008 and RC12WEE0003. (For interpretation of the references to color in this figure legend, the reader is referred to the web version of this article.)

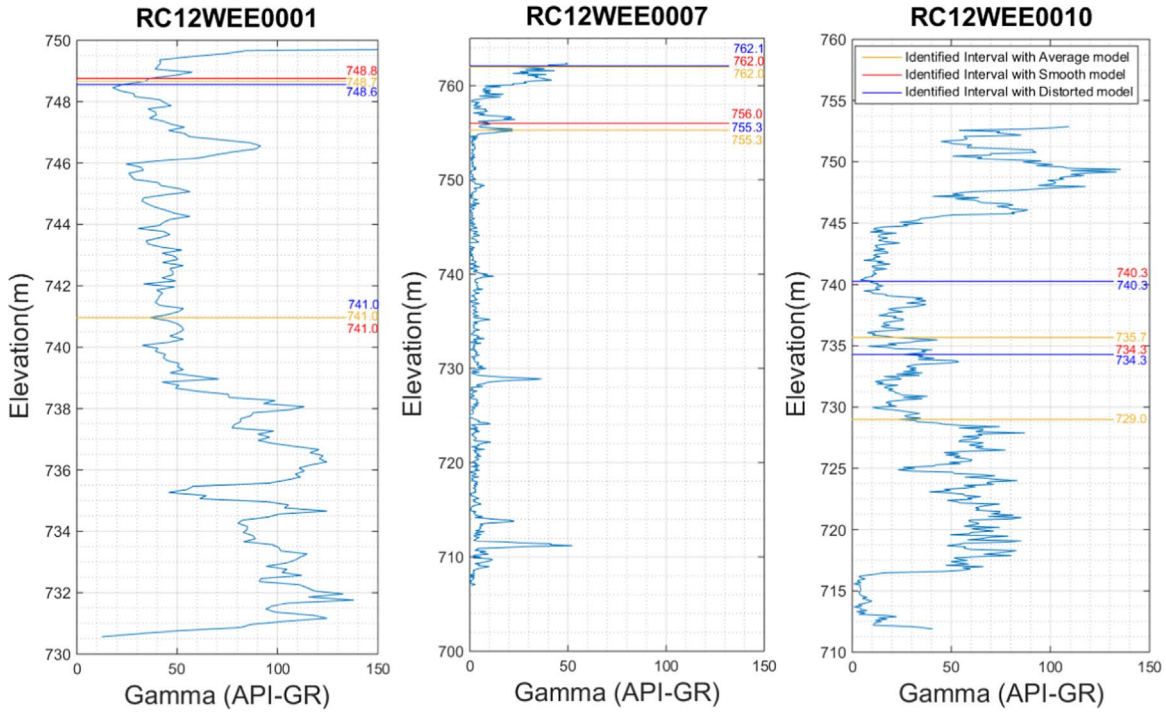

Fig. 12. Identified AS1-AS2 interval for holes that were interpreted to not contain the section.

Viterbi score for the Average and Smooth model. The uncertainties for the DTW distance and log MAP Viterbi score do not appear to be strongly impacted by the choice of model (average, smooth, or distorted) and preserve the ordering of the hole uncertainty well compared to the warping factor.

The plot of the actual % identification accuracy and against the uncertainties is presented in Fig. 13. The distorted model log MAP Viterbi uncertainty for RC12WEE0004 can be seen to be an outlier. This shows how characteristic signature uncertainty can be used to indicate the need for further geological investigation. Even though the identified interval has increased in accuracy compared to the average and smooth model, the uncertainty has also increased which indicates that the interval is anomalous compared to the model. This corresponds to the observation earlier that the anomalous natural gamma signature for rocks intersected by the RC12WEE0004 drill hole is likely related to the presence of an antiformal fold hinge.

4. Summary and future work

We present an application of a CPM that is capable of probabilistically modelling both the scale and alignment of a natural gamma signature of a shale marker. The characteristic signature that is learnt from this model can identify 98.72% of the gamma signatures of the AS1-AS2 shale marker interval of the West Angelas formation. While being limited to a dataset of 8 example signatures, the improvement over both the unaligned average model and the smooth model of identifying the entire interval for the RC12WEE0004 signature demonstrates the robustness of the model. This is also demonstrated by the range of windows used to search for the minimal DTW distance which were between 6.0 and 16.0 m at 0.1 m increments.

There are limitations and advantages of the profile HMM technique used in this research. The use of expectation-maximization to determine the optimal parameters can only determine the maximum likelihood estimate that is locally optimal and thus depends on the initial values. This also places limitations on having a measure of uncertainty since the posterior probability depends on the initial characteristic signature $\tilde{t}$ and the emission noise σ. The Bayesian approach for the inference of the posterior is usually in the form of Markov Chain Monte Carlo sampling (Listgarten et al., 2006) or variational inference (Wang and Blunsom, 2013), which would allow confidence intervals on the alignment to be constructed.

Another aspect that requires further work is assessing the uncer-

Table 3
Comparison of three uncertainty measures *for the identified intervals*: the minimal DTW distance, the warping factor, and the log MAP Viterbi score.

HoleID	DTW distance			Warping factor			log MAP viterbi score		
	Average	Smooth	Distorted	Average	Smooth	Distorted	Average	Smooth	Distorted
RC12WEE0001	1.50	1.22	0.98	0.38	0.40	0.43	−2700.33	−2688.80	−2750.21
RC12WEE0002	0.25	0.12	0.10	0.39	0.46	0.46	−462.79	−461.12	−463.29
RC12WEE0003	**0.27**	**0.13**	**0.07**	**0.40**	**0.39**	**0.36**	**−446.57**	**−453.18**	**−448.31**
RC12WEE0004	**0.34**	**0.22**	**0.17**	**0.47**	**0.44**	**0.51**	**−498.07**	**−506.32**	**−592.35**
RC12WEE0005	0.44	0.29	0.23	0.50	0.44	0.46	−482.31	−482.31	−482.31
RC12WEE0006	0.29	0.17	0.14	0.50	0.42	0.46	−458.15	−459.54	−461.29
RC12WEE0007	0.36	0.29	0.25	0.43	0.55	0.49	−513.75	−519.02	−506.82
RC12WEE0008	**0.27**	**0.10**	**0.08**	**0.43**	**0.41**	**0.43**	**−449.36**	**−450.76**	**−449.01**
RC12WEE0009	0.19	0.10	0.08	0.45	0.47	0.43	−446.01	−446.00	−448.47
RC12WEE0010	0.44	0.33	0.27	0.43	0.54	0.55	−661.48	−530.36	−530.36
RC12WEE0011	0.33	0.21	0.17	0.43	0.54	0.51	−477.04	−464.40	−465.50

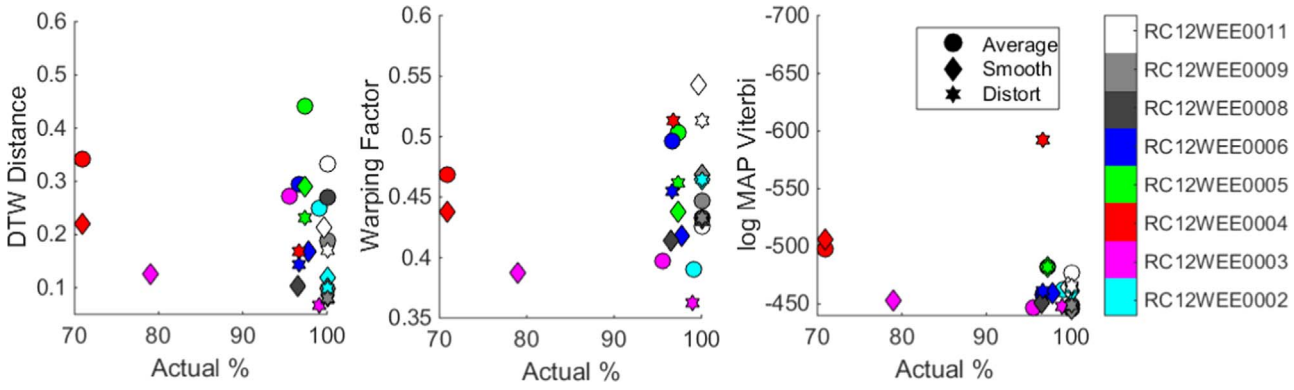

Fig. 13. Plot of the identified actual % accuracy (see Table 2) to the DTW distance (left), warping factor (middle) and log MAP Viterbi score (right).

tainty in signature identification, which is different from the uncertainty of the characteristic signature using the CPM which is developed in our work. Since we have made the identification of the signature by taking the interval with the minimal DTW distance, it is necessary to assume the existence of the characteristic signature in each log to generate a shale band horizon. However, for future work, our approach can be extended to test repeated or absent signatures in order to accommodate geological constraints such as faulting, folding and large erosional events. We suggest that the identification of these types of signatures and the uncertainty associated with them is more suitably framed as a propagation of geological prior information (Wood and Curtis, 2004). How characteristic signature uncertainty can be incorporated with geological prior information –such as the shale bands dip and strike measurements or the structural setting– for modelling is an area we intend to further investigate.

The main benefits of using profile HMM in geological applications is in the specification of a consensus sequence, which can be thought of as analogous to a stratigraphic sequence. Existing approaches to automated stratigraphic alignment are usually based on some variation of DTW (Collins and Doveton, 1994), which while effective in measuring sequence similarity, do not have a probabilistic formulation which allows it to learn a characteristic signature or stratigraphic column. This is due to DTW treating every position in a sequence as equally likely to warp. The uncertainty in alignment can be calculated formally in profile HMM which also allow multiple realization of the alignment to be made since the joint probability is inferred. The prior probability of transitions can also be made based on correlation rules like paleoangle consistency and sedimentary profile consistency, as in Lallier et al. (2016), to incorporate stratigraphic knowledge.

Further work is required to determine how the complexity of the geometry of the ore body contacts has an impact on the resource estimation. Since drillhole spacing is at a much finer resolution at the stage of resource estimation, the accuracy of the correctly identifying the ore body contact has direct effect on the uncertainty of the estimate which is commonly unfolded before estimation in tabular ore bodies (Sommerville et al., 2014). We intend to investigate further how geostatistical estimation uncertainty (Strebelle, 2002) and geometry uncertainty can be further incorporated.

Acknowledgments

Paul Duuring publishes with permission from the Director of the Geological Survey of Western Australia.

References

Abzalov, M., 2016. Geological constraints of mineralisation. In: Applied Mining Geology. Springer International Publishing, pp. 193–205.

Baum, L.E., Petrie, T., Soules, G., Weiss, N., 1970. A maximization technique occurring in the statistical analysis of probabilistic functions of Markov chains. Ann. Math. Stat. 41, 164–171.

Blockley J.G., 1979. A Contribution to the Stratigraphy of the Marra Mamba Iron Formation. Geological Survey of Western Australia.

Blockley J.G., Tehnas I.J., Mandyczewsky A., Morris R.C., 1993. Proposed stratigraphic subdivisions of the Marra Mamba Iron Formation and the lower Wittenoom Dolomite, Hamersley Group, Western Australia. Geological Survey of Western Australia.

Borsaru, M., Zhou, B., Aizawa, T., et al., 2006. Automated lithology prediction from PGNAA and other geophysical logs. Appl. Radiat. Isot. 64, 272–282. http://dx.doi.org/10.1016/j.apradiso.2005.07.012.

Carle, S.F., Fogg, G.E., 1997. Modeling spatial variability with one and multidimensional continuous-lag Markov Chains. Math. Geol. 29, 891–918. http://dx.doi.org/10.1023/A:1022303706942.

Chang, H., Kopaska-Merkel, D.C., Chen, H.-C., Durrans, S.R., 2000. Lithofacies identification using multiple adaptive resonance theory neural networks and group decision expert system. Comput. Geosci. 26, 591–601. http://dx.doi.org/10.1016/S0098-3004(00)00010-8.

Clout, J.M.F., 2006. Iron formation-hosted iron ores in the Hamersley Province of Western Australia. Appl. Earth Sci. 115, 115–125. http://dx.doi.org/10.1179/174327506X138931.

Clout, J.M.F., Simonson, B.M., 2005. Precambrian iron formations and iron formation-hosted iron ore deposits. Econ. Geol. One Hundredth Anniv. 1905–2005, 643–679. http://dx.doi.org/10.5382/AV100.20.

Collins, D.R., Doveton, J.H., 1994. Automated correlation based on markov analysis of vertical succession and Walther's Law. In: Computers in Geology 25 Years of Progress. Oxford University Press, Cary, pp. 121–132.

Dempster, A.P., Laird, N.M., Rubin, D.B., 1977. Maximum Likelihood from incomplete data via the EM algorithm. J. R. Stat. Soc. Ser. B Methodol. 39, 1–38.

Doveton, J.H., 1971. An application of Markov chain analysis to the Ayrshire coal measures succession. Scott. J. Geol. 7, 11–27. http://dx.doi.org/10.1144/sjg07010011.

Durbin, R., 1998. Biological Sequence Analysis Probabilistic Models of Proteins and Nucleic Acids. Cambridge University Press, Cambridge.

Eidsvik, J., Mukerji, T., Switzer, P., 2004. Estimation of geological attributes from a well log: an application of hidden Markov Chains. Math. Geol. 36, 379–397. http://dx.doi.org/10.1023/B:MATG.0000028443.75501.d9.

Forney, G.D., 1973. The Viterbi algorithm. Proc. IEEE 61, 268–278. http://dx.doi.org/10.1109/PROC.1973.9030.

Geological Survey of Western Australia, 2016. 1:500 000 State interpreted bedrock geology of Western Australia, 2016.

Horrocks, T., Holden, E.-J., Wedge, D., 2015. Evaluation of automated lithology classification architectures using highly-sampled wireline logs for coal exploration. Comput. Geosci. 83, 209–218. http://dx.doi.org/10.1016/j.cageo.2015.07.013.

Insua, T.L., Hamel, L., Moran, K., et al., 2015. Advanced classification of carbonate sediments based on physical properties. Sedimentology 62, 590–606. http://dx.doi.org/10.1111/sed.12168.

Jeong, J., Park, E., Han, W.S., Kim, K.-Y., 2014. A novel data assimilation methodology for predicting lithology based on sequence labeling algorithms. J. Geophys. Res. Solid Earth 119. http://dx.doi.org/10.1002/2014JB011279.

Jones, H., Walraven, F., Knott, G.G., 1973. Natural gamma logging as an aid to iron ore exploration in the Pilbara region of Western Australia. AusIMM, 53–60.

Keogh, E., Ratanamahatana, C.A., 2004. Exact indexing of dynamic time warping. Knowl. Inf. Syst. 7, 358–386. http://dx.doi.org/10.1007/s10115-004-0154-9.

Kneeshaw, M., Kepert, D.A., Tehnas, I.J., Pudovskis, M.A., 2003. From Mount Goldsworthy to Area C – reflections on forty years of iron ore exploration in the Pilbara. Appl. Earth Sci. 112, 38–55. http://dx.doi.org/10.1179/037174503225011207.

Lallier, F., Caumon, G., Borgomano, J., et al., 2016. Uncertainty assessment in the stratigraphic well correlation of a carbonate ramp: method and application to the Beausset Basin, SE France. Comptes Rendus Geosci. 348, 499–509. http://dx.doi.org/10.1016/j.crte.2015.10.002.

Lin, L., Khider, D., Lisiecki, L.E., Lawrence, C.E., 2014. Probabilistic sequence alignment of stratigraphic records. Paleoceanography 29. http://dx.doi.org/10.1002/2014PA002713.

Lindberg, D.V., Grana, D., 2015. Petro-elastic log-facies classification using the expectation–maximization algorithm and hidden Markov models. Math. Geosci. 47,

719–752. http://dx.doi.org/10.1007/s11004-015-9604-z.
Listgarten, J., Neal, R.M., Roweis, S.T., et al., 2006. Bayesian detection of infrequent differences in sets of time series with shared structure. Adv. Neural Inf. Process. Syst., 905–912.
Listgarten, J., Neal, R.M., Roweis, S.T., Emili, A., 2004. Multiple alignment of continuous time series. Adv. Neural Inf. Process. Syst., 817–824.
Murphy, R.J., Silversides, K.L., 2017. Investigating variations in background response in measurements of downhole natural gamma in a banded iron formation in the Pilbara, Western Australia. J. Appl. Geophys. 137, 118–127. http://dx.doi.org/10.1016/j.jappgeo.2016.12.018.
Qi, L., Carr, T.R., 2006. Neural network prediction of carbonate lithofacies from well logs, Big Bow and Sand Arroyo Creek fields, Southwest Kansas. Comput. Geosci. 32, 947–964. http://dx.doi.org/10.1016/j.cageo.2005.10.020.
Rabiner, L.R., 1989. A tutorial on hidden Markov models and selected applications in speech recognition. Proc. IEEE 77, 257–286. http://dx.doi.org/10.1109/5.18626.
Rider, M.H., 1990. Gamma-ray log shape used as a facies indicator: critical analysis of an oversimplified methodology. Geol. Soc. Lond. Spec. Publ. 48, 27–37. http://dx.doi.org/10.1144/GSL.SP.1990.048.01.04.
Rider M.H., 1996. The Geological Interpretation of Well Logs, 2nd ed. Caithness, Scotland, Whittles, Caithness, Scotland.
Russell, W.L., 1941. Well logging by radioactivity. AAPG Bull. 25, 1768–1788.
Sakoe, H., Chiba, S., 1978. Dynamic programming algorithm optimization for spoken word recognition. IEEE Trans. Acoust. Speech Signal Process 26, 43–49. http://dx.doi.org/10.1109/TASSP.1978.1163055.
Schlanser, K., Grana, D., Campbell-Stone, E., 2016. Lithofacies classification in the Marcellus Shale by applying a statistical clustering algorithm to petrophysical and elastic well logs. Interpretation 4, SE31–SE49. http://dx.doi.org/10.1190/INT-2015-0128.1.
Silversides, K., Melkumyan, A., Wyman, D., Hatherly, P., 2015a. Automated recognition of stratigraphic marker shales from geophysical logs in iron ore deposits. Comput. Geosci. 77, 118–125. http://dx.doi.org/10.1016/j.cageo.2015.02.002.
Silversides, K.L., Melkumyan, A., 2016a. Robust library building for autonomous classification of downhole geophysical logs using Gaussian processes. Pure Appl. Geophys., 1–14. http://dx.doi.org/10.1007/s00024-016-1459-9.
Silversides, K.L., Melkumyan, A., 2016b. A dynamic time warping based covariance function for Gaussian processes signature identification. Comput. Geosci. 96, 69–76. http://dx.doi.org/10.1016/j.cageo.2016.08.001.
Silversides, K.L., Melkumyan, A., Wyman, D., 2015b. Fusing Gaussian processes and dynamic time warping for improved natural gamma signal classification. Math. Geosci. 48, 187–210. http://dx.doi.org/10.1007/s11004-015-9601-2.
Silversides K.L., Melkumyan A., Wyman D.A., , et al., 2011. Detection of geological structure using gamma logs for autonomous mining. In: 2011 IEEE International Conference on Robotics and Automation (ICRA). pp 1577–1582.
Sommerville, B., Boyle, C., Brajkovich, N., et al., 2014. Mineral resource estimation of the Brockman 4 iron ore deposit in the Pilbara region. Appl. Earth Sci. 123, 135–145. http://dx.doi.org/10.1179/1743275814Y.0000000038.
Srivastava, R.M., 2005. Probabilistic modeling of ore lens geometry: an alternative to deterministic wireframes. Math. Geol. 37, 513–544. http://dx.doi.org/10.1007/s11004-005-6670-7.
Strebelle, S., 2002. Conditional simulation of complex geological structures using multiple-point statistics. Math. Geol. 34, 1–21. http://dx.doi.org/10.1023/A:1014009426274.
Taylor, D., Dalstra, H.J., Harding, A.E., et al., 2001. Genesis of high-grade hematite orebodies of the Hamersley Province, Western Australia. Econ. Geol. 96, 837–873. http://dx.doi.org/10.2113/gsecongeo.96.4.837.
Thorne, W., Hagemann, S., Webb, A., Clout, J., 2008. Banded iron formation-related iron ore deposits of the Hamersley Province, Western Australia. In: Banded Iron Formation-Related High-Grade Iron Ore. Society of Economic Geologists, pp. 197–221.
Wainwright, M.J., Jordan, M.I., 2008. Graphical models, exponential families, and variational inference. Found. Trends Mach. Learn. 1, 1–305. http://dx.doi.org/10.1561/2200000001.
Wang, G., Carr, T.R., 2012. Marcellus shale lithofacies prediction by multiclass neural network classification in the Appalachian Basin. Math. Geosci. 44, 975–1004. http://dx.doi.org/10.1007/s11004-012-9421-6.
Wang, P., Blunsom, P., 2013. Collapsed variational Bayesian inference for hidden Markov models. J. Mach. Learn. Res. 31, 599–607.
Wood, R., Curtis, A., 2004. Geological prior information and its applications to geoscientific problems. Geol. Soc. Lond. Spec. Publ. 239, 1–14. http://dx.doi.org/10.1144/GSL.SP.2004.239.01.01.